Corrosion-induced changes in the serviceability behavior of reinforced concrete beams under cyclic loading

Citation for the original published paper (version of record):
Dackman, D., Gil Berrocal, C., Rempling, R. et al (2026). Corrosion-induced changes in the serviceability behavior of reinforced concrete beams under cyclic loading. Structures, 91. http://dx.doi.org/10.1016/j.istruc.2026.112605

(article starts on next page)

Structures 91 (2026) 112605

Contents lists available at ScienceDirect

Structures

journal homepage: www.elsevier.com/locate/structures

Corrosion-induced changes in the serviceability behavior of reinforced concrete beams under cyclic loading

David Dackman [a,b,*], Carlos G. Berrocal [a], Rasmus Rempling [a,c], Ignasi Fernandez [a]

[a] Chalmers University of Technology, Division of Structural Engineering, Göteborg 41296, Sweden
[b] WSP Sverige AB, Fabriksgatan 2, Göteborg 41250, Sweden
[c] NCC Sverige AB, Drakegatan 10, Göteborg 41250, Sweden

ARTICLE INFO

Keywords:
Reinforced Concrete
Corrosion
Serviceability response
Distributed optic fiber sensing (DOFS)

ABSTRACT

Understanding the development of reinforcement corrosion and its effects on the service life of reinforced concrete (RC) structures remains a critical challenge, accompanied by significant uncertainties. Corrosion is one of the most prevalent deterioration mechanisms in RC infrastructure, leading to reduced structural performance, increased maintenance costs, and serious safety concerns. Previous studies have investigated the influence of corrosion on the structural response of RC members, while distributed optical fiber sensing (DOFS) has emerged as a promising technique for monitoring strains, cracking, and deflection in RC structures. Earlier research has also demonstrated the potential of DOFS-based deflection measurements for characterizing localized corrosion propagation. However, the applicability of such approaches under varying reinforcement configurations and corrosion conditions remains insufficiently understood. In this study, the serviceability response of RC beams subjected to cyclic loading and accelerated corrosion was investigated using DOFS measurements. A previously developed framework for describing corrosion propagation based on corrosion-induced deflections was validated and extended to different reinforcement diameters, bar arrangements, and corroded regions. The results showed that the framework became less accurate when corrosion was more uniformly distributed rather than localized in pits. Furthermore, a detailed analysis of the strain evolution at a representative cracked section revealed that corrosion-induced non-mechanical strains propagated throughout the cross-section until longitudinal cracking occurred. Subsequently, an apparent Young's modulus derived from sectional strain distributions proved to be a useful indicator of corrosion progression.

1. Introduction

Reinforced concrete (RC) is the most widely used material in infrastructure construction today. However, the durability of many RC structures is increasingly compromised by aging, ongoing deterioration processes, and increasing traffic loads. Moreover, the deterioration of concrete structures worldwide has been significantly affected by climate change and increasing CO_2 emissions [1,2]. Since replacing all deficient structures is neither economically realistic nor environmentally sustainable, extending their service life requires effective maintenance strategies and reliable condition assessment methods.

Among the deterioration mechanisms affecting RC, reinforcement corrosion is the most prevalent and costly [3], estimated to account for more than 40% of global infrastructure repair costs [4]. Recent catastrophic failures, including the collapses of the I-35W Bridge in Minneapolis [5] and the Morandi Bridge in Genoa [6], have further highlighted the severe risks associated with corrosion-induced degradation. In addition to the direct costs of corrosion, the environmental impact is also substantial. Recent estimates suggest that replacing steel lost to corrosion could account for roughly 4–9% of global CO_2 emissions by 2030 under current practices [7].

Corrosion initiates once the protective passive film on the steel surface is destroyed, either through carbonation of the concrete cover or through chloride ingress. This process ultimately reduces both the steel cross-sectional area and the bond between steel and concrete [8,9]. Due to uncertainties in environmental exposure, loading conditions and material properties, the remaining service life of RC structures is inherently uncertain. To account for these aspects, Kopiika et al. [10] incorporated probabilistic modeling to assess the probability of failure and residual service life under varying exposure conditions.

* Corresponding author at: Chalmers University of Technology, Division of Structural Engineering, Göteborg 41296, Sweden.
E-mail address: david.dackman@chalmers.se (D. Dackman).

https://doi.org/10.1016/j.istruc.2026.112605
Received 17 March 2026; Received in revised form 6 July 2026; Accepted 7 July 2026
Available online 9 July 2026

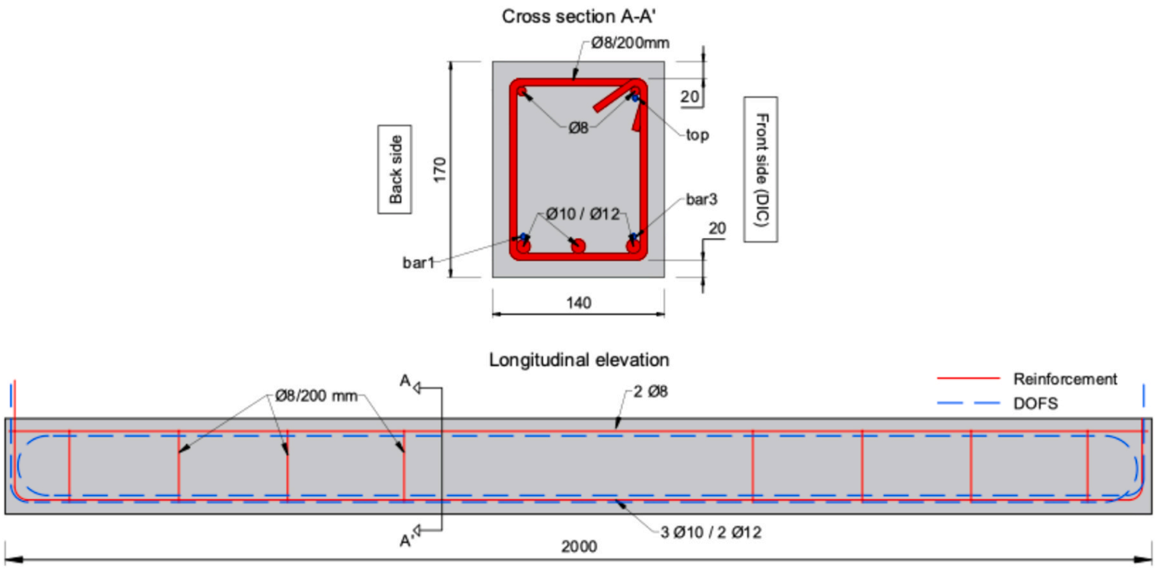

Fig. 1. Reinforcement layout, DOFS configuration and geometry of the beam specimen (all measurements in mm).

Table 1
Reinforcement layout, region subjected to corrosion and applied current.

Specimen	ϕ [mm]	n_ϕ	Corroded region	I [A]
Beam 1-s1 Beam 1-s2	12	2	-	-
Beam 5-s1 Beam 5-s2	12	2	Whole beam	0.08
Beam 2-s1 Beam 2-s2	12	2	-	-
Beam 6-s1 Beam 6-s2	12	2	Constant-moment span	0.03
Beam 3-s1 Beam 3-s2	10	3	-	-
Beam 7-s1 Beam 7-s2	10	3	Whole beam	0.10
Beam 4-s1 Beam 4-s2	10	3	-	-
Beam 8-s1 Beam 8-s2	10	3	Constant-moment span	0.04

Over the past decades, considerable research has focused on how corrosion influences the structural response of RC [11,12,13,14]. Zhang et al. [15] studied beams subjected to natural corrosion for 14–23 years under service loading. Corrosion simulations intended to replicate the behavior of the naturally corroded beams suggested that increases in deflection in the early cracking stage were governed primarily by bond deterioration, whereas cross-sectional area loss became relevant only at later stages after significant bond degradation and the development of generalized corrosion.

Stein et al. [11] investigated how corrosion influences the structural behavior of RC beams subjected to cyclic loading. Corrosion was induced by impressed current to achieve 3–5% and 8–11% steel mass losses. At the higher corrosion level, displacement growth was larger than in both the uncorroded and lightly corroded specimens. However, beams subjected to the lower corrosion level displayed a smaller increase in average vertical displacement than the uncorroded references, likely due to bond-stiffness improvement from corrosion-product pressure. Similar behavior was observed for the bond strength in a study by Fang et al. [16], when pull-out tests were carried out to study the bond stress-slip response for different corrosion levels and loading histories. An increase in corrosion level enhanced bond strength up to a certain threshold, beyond which the strength was significantly reduced.

Malumbela et al. [17] investigated the cross-sectional behavior of RC beams subjected to accelerated corrosion under sustained service loads, using mechanical strain gauges. The results showed that tensile strains increased with time for all corroded specimens, while compressive strain development depended on the load level. Beams without transverse cracking exhibited increases in both compressive and tensile strains, whereas the beam with higher load level, and consequently transverse cracks, showed compressive strains that stabilized after an initial increase. In the latter case, the neutral axis depth progressively decreased until approaching the cover of the compression reinforcement, after which it remained constant.

Conventional strain-measurement techniques provide information only at discrete locations. This limitation has been addressed through the development of Distributed Optical Fiber Sensors (DOFS), which offer continuous strain profiles. Beyond overcoming spatial limitations, DOFS also provide advantages over traditional structural health monitoring systems, such as compact geometry, immunity to electromagnetic interference, high sensitivity, and inherent corrosion resistance. DOFS have been shown to effectively monitor structural indicators such as deflection, cracking, and strain fields in RC members [18,19,20,21,22,23]. Furthermore, they have been applied to study bond stress–slip behavior [24] and to characterize corrosion processes, where strain-based measurements identified corrosion stages consistent with electrochemical data [25].

While previous research has highlighted the capability of DOFS to monitor performance indicators in RC elements, studies directly linking these measurements to corrosion-related damage remain limited. Building upon the framework proposed in previous work [26,27], which linked DOFS-based deflection measurements to localized pitting corrosion propagation, the present study seeks to validate and extend its applicability under broader conditions. Specifically, the influence of reinforcement diameter, number of bars, and extent of the corroded region on the structural behavior is examined through a new series of tests. In addition, a more detailed analysis of the cross-sectional response is undertaken to capture how it is affected by corrosion damage. Consequently, this study extends the previously proposed framework and provides further evidence of the potential of DOFS for characterizing corrosion progression and its structural consequences.

2. Experimental program

The experimental program presented in this paper comprised 16 beams divided into two test series, designed to evaluate the use of DOFS

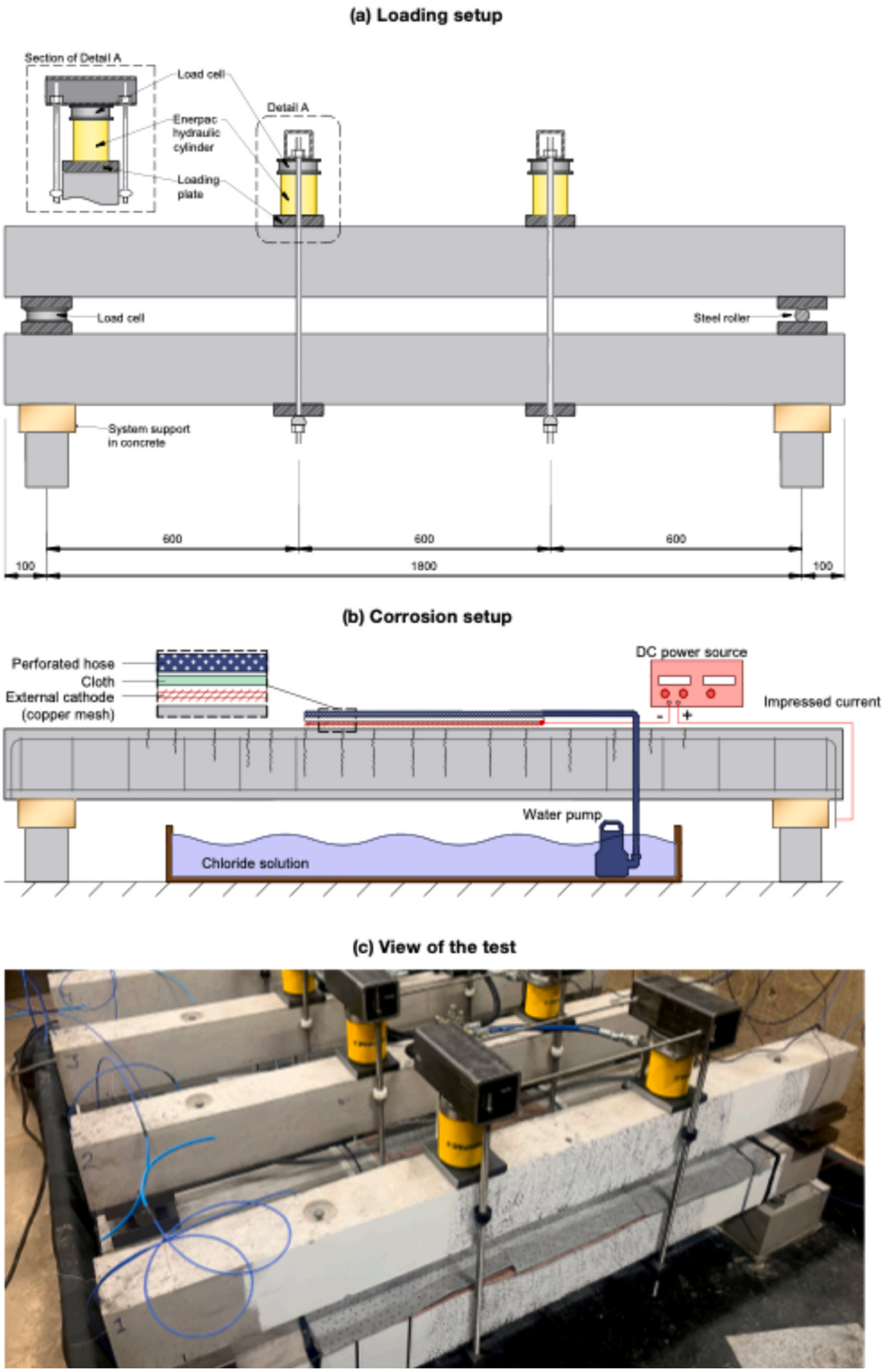

Fig. 2. **(a)** Long-term loading setup; **(b)** Accelerated corrosion setup utilizing impressed current; **(c)** View of the test setup (all measurements are in mm).

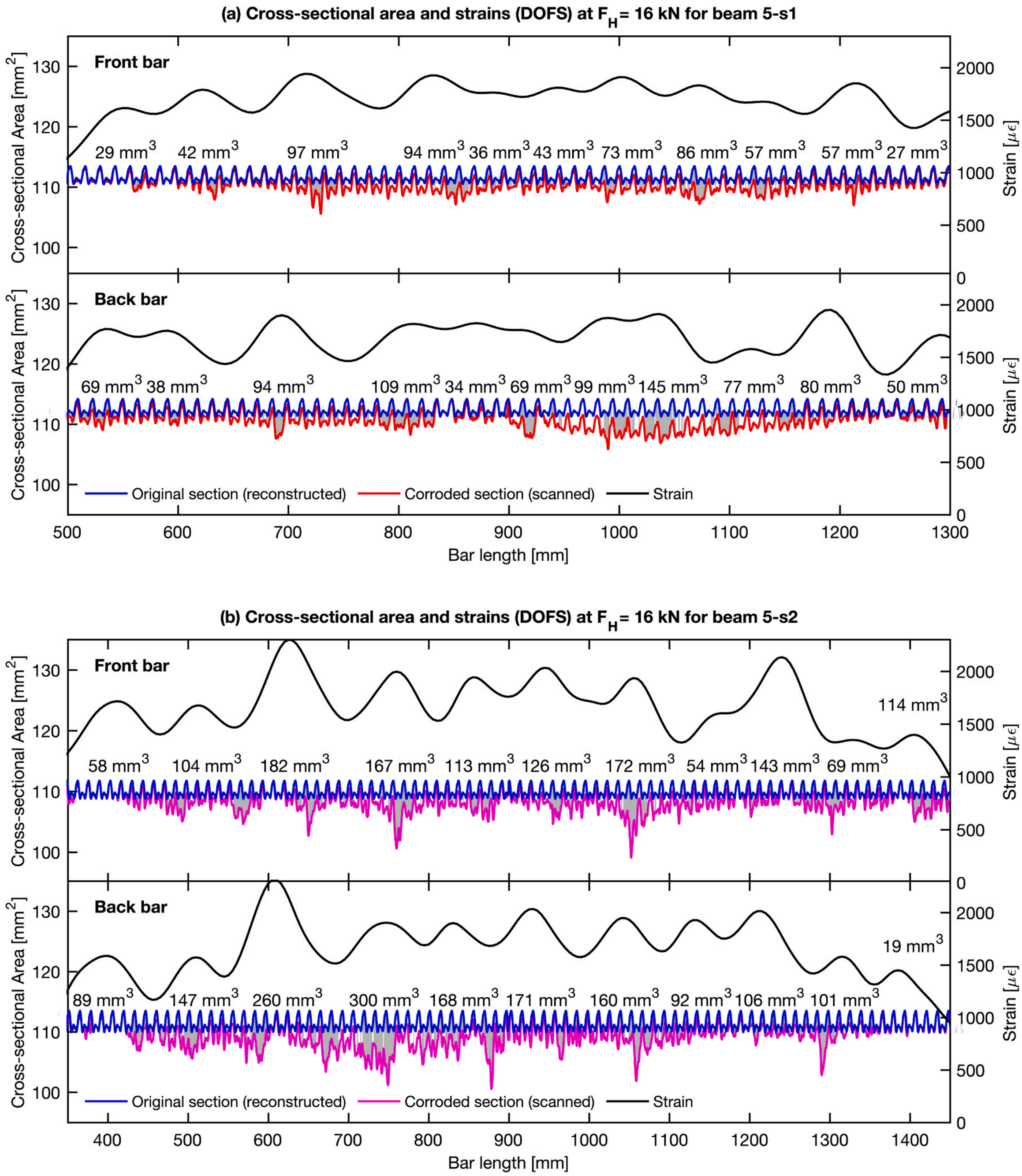

Fig. 3. **(a)** Variation of residual and original cross-sectional area along the rebars, together with pit volume of each pit and strains for a load cycle with maximum load, $F_H = 16$ kN, in beam 5-s1; **(b)** Variation of residual and original cross-sectional area along the rebars, together with pit volume of each pit and strains for a load cycle with maximum load, $F_H = 16$ kN, in beam 5-s2.

Table 2
Steel volume loss due to pitting corrosion, total steel volume losses, the ratio between them and the effective current.

Specimen	$C_{pit,scan}$ [mm^3]	$C_{tot,scan}$ [mm^3]	$C_{pit,scan}$ / $C_{tot,scan}$ [%]	I_{eff} [A]
Beam 5-s1	1506	2502	60	0.026
Beam 5-s2	2914	4217	69	0.020
Beam 6-s1	1098	1700	65	0.019
Beam 6-s2	2023	3194	63	0.015
Beam 7-s1	2074	3154	66	0.036
Beam 7-s2	5386	8526	63	0.071
Beam 8-s1	1594	2485	64	0.027
Beam 8-s2	2167	3558	61	0.028

for monitoring RC beam performance under long-term loading and deterioration. The test setup aimed to reproduce the configuration described in [27], while certain parameters were varied across the present beams. After initial pre-cracking, the specimens in this study were cyclically loaded, while simultaneously subjected to accelerated corrosion through impressed current. The two series differed only in the duration of the accelerated corrosion phase. The experimental program is described below, together with the deviations from the configuration in [27], as new analyses from results reported in earlier tests are also included in Section 4.2.

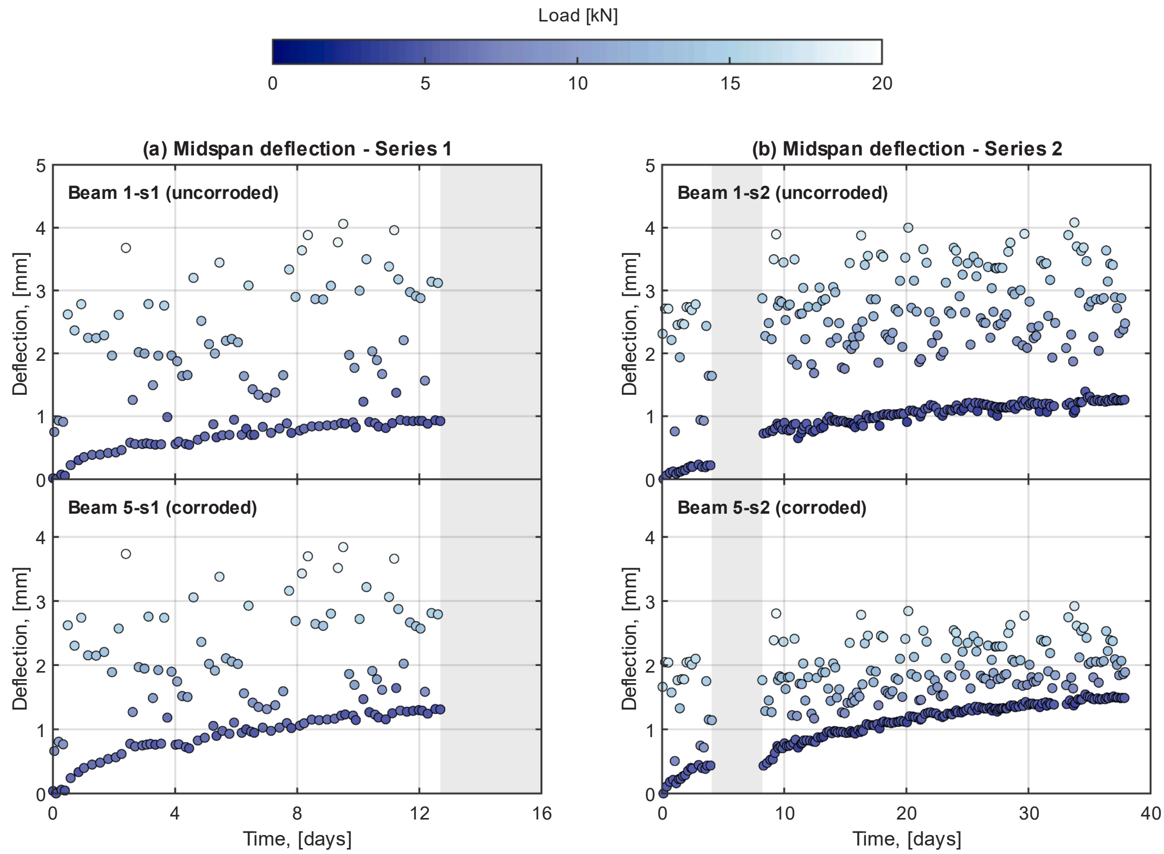

Fig. 4. (a) Midspan deflection measured by the DOFS for beam 1-s1 and beam 5-s1; **(b)** Midspan deflection measured by the DOFS for beam 1-s2 and beam 5-s2.

2.1. Geometry and reinforcement layout

RC beam specimens with a rectangular cross-section of 140 × 170 mm and a length of 2 m were used in the study. All reinforcement bars consisted of normal-ductility carbon steel (B500C) and to improve anchorage, the ends of the bottom longitudinal bars were bent upward. Moreover, at one end of the beam, the reinforcement bars protruded to enable electrical connection during the accelerated corrosion. The specimen geometry and bar arrangement are shown in Fig. 1.

Reinforcement layouts were selected to maintain approximately the same longitudinal reinforcement ratio while varying the bar diameter and the bar count. Details of the different reinforcement layouts are provided in Table 1, together with accelerated corrosion parameters described in Section 2.2. In comparison, the study in [27] featured beams with a total length of 3 m, a rectangular cross-section of 200 × 250 mm and tensile reinforcement consisting of three ⌀16 mm bars.

A water-to-cement ratio of 0.45 was used in the concrete mix, and a sulfate-resistant Portland cement with moderate heat release and low C_3A was used. Compressive strength tests performed, according to EN 12390–3:2009 on three 150 mm cubes, yielded 28-day mean values of 59.9 MPa (CoV = 4.6%) for Series 1 and 52.2 MPa (CoV = 1.4%) for Series 2.

2.2. Test setup and instrumentation

The beams were clamped together in pairs and tested in four-point bending, with pre-cracking introduced by two load cycles before the onset of long-term loading and accelerated corrosion after 28 days. The bottom beam was turned upside down to expose the tensile side upward, after which the top beam was placed on plates supported by the lower beam, as shown in Fig. 2a. The supports were located 1800 mm apart and loading points were introduced by placing hydraulic cylinders between each clamping device and the loading plates of the top beam according to Detail A in Fig. 2a. All beams were subjected to cyclic loading, following a square wave signal in which the cycle amplitude and duration varied randomly within predefined intervals. The maximum load per cycle, F_H, ranged from 8 to 16 kN for each cylinder, with pulse durations spanning from 1 to 6 h. Between the high load cycles, a constant load of $F_L = 6$ kN was applied for 1 h.

An impressed current was applied to the bottom beam to initiate the corrosion process and then held constant over the entire test. The tensile reinforcement was electrically connected and wired to the positive terminal of a DC supply, while a copper mesh on the tensile side was connected to the negative terminal to serve as an external cathode. During testing, cloth placed over the mesh was periodically wetted to maintain the electrolyte path, and a 0.5% NaCl solution (by mass) was pumped from a reservoir beneath the beam every 30 min for 5 min. The configuration shown in Fig. 2b, in combination with the pre-cracking, was chosen to promote non-uniform corrosion with distinct pits, as the cracks would provide paths of least resistance. A general view of the test setup is shown in Fig. 2c.

Two configurations of the corroded region were considered, either confined to the constant-moment span or covering almost the entire beam according to Table 1. For each specimen, the applied current was selected so that the current density was approximately equal across the beams, accounting for reinforcement diameter and the number of cracks exposed to corrosion. For Series 1, corrosion was applied until longitudinal cracking was observed after 16 days, while Series 2 was subjected to corrosion for 40 days. For comparison, the study in [27] considered specimens with corrosion confined to the same region, namely the constant-moment span, and were tested for 67 days.

DOFS were used for continuous strain measurements along the specimens. In Series 1, one fiber per beam was installed in a multilayer

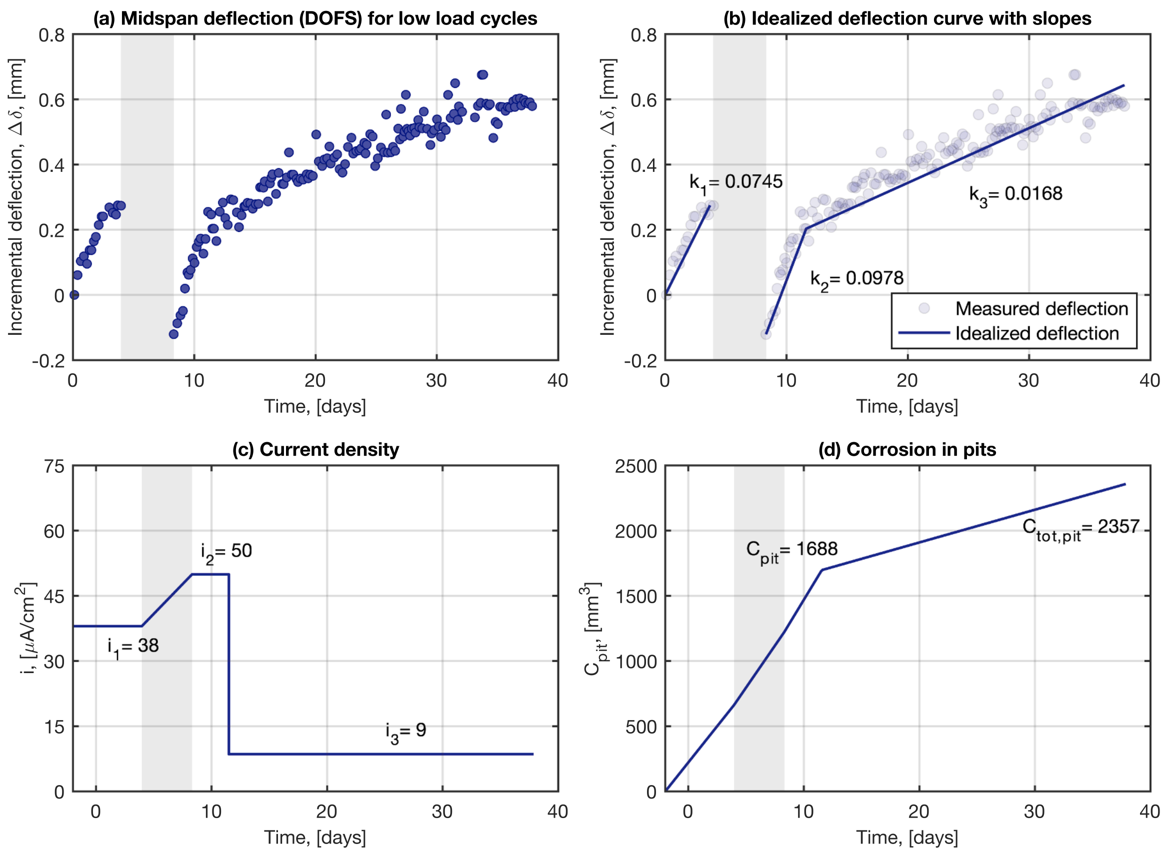

Fig. 5. **(a)** Midspan deflection of beam 5-s2 measured by the DOFS for low load cycles, $F_L = 6$ kN; **(b)** An idealized curve of the deflection with the slopes of each stage; **(c)** Current densities for the different stages; **(d)** Total corrosion in the pits calculated with Faraday's law.

Table 3
3D-scanned steel volume loss due to pitting corrosion, calculated steel volume losses and the ratio between them.

Specimen	$C_{tot.pit}$ [mm^3]	$C_{pit.scan}$ [mm^3]	$C_{tot.pit}$ / $C_{pit.scan}$ [%]
Beam 5-s2	2357	2914	81
Beam 6-s2	1630	2023	81
Beam 7-s2	4798	5386	89
Beam 8-s2	1945	2167	90

configuration by securing the cable to the reinforcement bars with electrical tape according to Fig. 1. In Series 2, only four channels were available in the acquisition system and consequently, one fiber was allocated to each beam pair and connected in series. The fiber cable used for strain monitoring was BRUsens V9 from Solifos. The relatively robust cable consists of a 3.2 mm polyamide outer jacket, a 0.9 mm steel tube, and a multilayer buffer that enhances strain transfer, enclosing a 250 μm single-mode optical fiber. Strain data were recorded using a Luna ODiSI 6000 optical distributed sensing interrogator. Measurements were acquired at a rate of one sample every 10 min with a spatial resolution of 2.6 mm between gauge points. Prior to analysis, the raw profiles were resampled by applying cubic Hermite interpolation to generate a 10 mm spatial grid, thereby reducing the data volume while retaining the accuracy of the measurements, as shown in [22].

2.3. Characterization of the resulting rebar corrosion

To assess the corrosion damage, the tensile-side concrete cover was removed to reveal the reinforcement. Rebar sections from the corroded regions were then cut using a water-cooled circular saw, after which remaining corrosion products were cleaned by sandblasting as described in [28]. The bar segments were laser-scanned in 3D with a portable HandySCAN 700™ laser scanner from Creaform to produce a point cloud with an accuracy of 30 μm and a maximum spatial resolution of 0.05 mm.

The point cloud was surface interpolated according to [29], after which cross-sectional areas were obtained from surface point integration. Integrating the resulting local area losses over the bar length yielded the total volume loss according to Eq. (1):

$$C_{tot,scan} = \int_0^{L_{bar}} (A_0(x) - A_{corr}(x))dx \tag{1}$$

where L_{bar} is the extracted bar length, A_0 is the uncorroded cross-sectional area and A_{corr} is the corroded cross-sectional area.

Furthermore, the average corrosion level was evaluated over the mean crack spacing. Localized pitting regions were subsequently identified following the method in [30], where the pit length was defined as the distance over which the local corrosion level exceeded the average level. The pit corrosion volume, $C_{pit,scan}$, was then obtained by integrating the local sectional loss along the pit length, according to Eq. (2):

$$C_{pit,scan} = \sum_{i=1}^{n_{pit}} \int_{x_{pit\_start_i}}^{x_{pit\_end_i}} (A_0(x) - A_{corr}(x))dx \tag{2}$$

where n_{pit} is the total number of pits and $L_{pit} = x_{pit\_end} - x_{pit\_start}$ is the pit length.

3. Framework for describing corrosion propagation from corrosion-induced variations in deflection

The authors proposed a framework to describe corrosion development in reinforced concrete beams by linking it to corrosion-induced

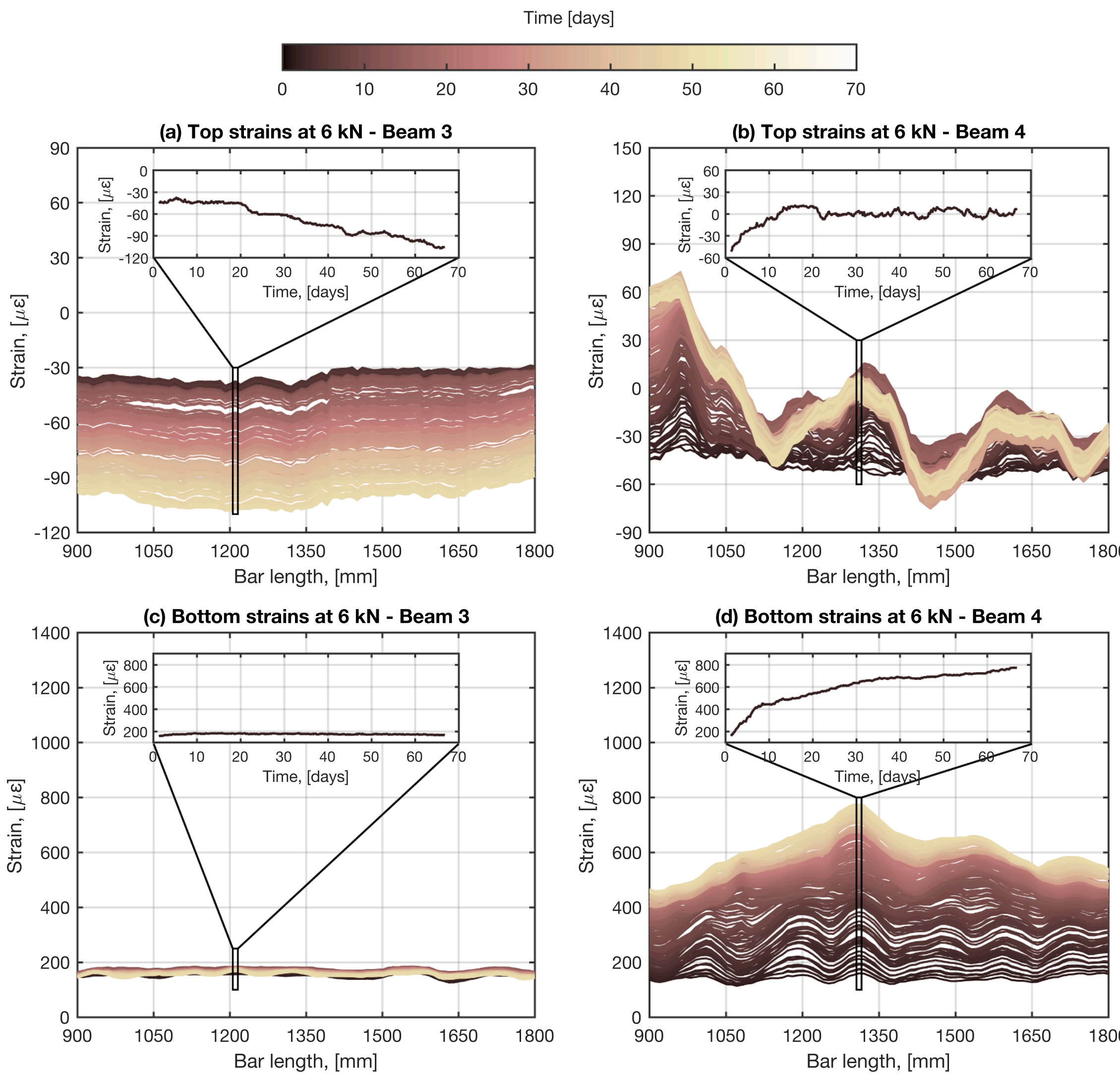

Fig. 6. **(a, b)** Strains along the top reinforcement bar for load cycles $F_L = 6$ kN, in beam 3 (uncorroded) and beam 4 (corroded) from [27]; **(c, d)** Strains along the bottom reinforcement bar for load cycles $F_L = 6$ kN, in beam 3 (uncorroded) and beam 4 (corroded) from [27].

deflections in [26,27]. Strain data obtained from the DOFS were used to compute deflections over time and once the initial current density had been established, the framework enabled the estimation of corrosion development solely from the measured deflection response using Faraday's law. The calculation of the final corroded steel volume was based on an underlying hypothesis and two assumptions. The hypothesis states that any measurable change in deflection is attributed exclusively to corrosion occurring at crack-associated pits, implying a proportional relationship between deflection magnitudes and the extent of steel loss. The first assumption states that, prior to the initiation of longitudinal cracking, corrosion is entirely concentrated at the cracks. The second assumption introduces an influence region surrounding each pit that governs deflection variations, expressed as an effective pit length, which is further assumed to remain constant over time.

An effective impressed current I_{eff} was calculated employing Faraday's law and the total measured volume loss obtained from the 3D scanning, as stated in Eq. (3):

$$I_{eff} = \frac{C_{tot,scan}}{C_{tot,Faraday}} \bullet I = \frac{C_{tot,scan}}{\frac{\Delta m}{\rho}} \bullet I = \frac{C_{tot,scan}}{\frac{Mt}{\rho Fz}} \quad (3)$$

where $C_{tot,scan}$ is the total corrosion volume for all three bars obtained from the 3D scanning, $C_{tot,Faraday}$ is the total corrosion volume according to Faraday's law, Δm is the mass loss of steel, ρ is the density of iron, M is the atomic weight of iron, I is the current, t is time of applied current, F is the Faraday's constant and z is the valency of Fe.

Based on the first assumption, the current density at the initiation of the corrosion process, i_1, can be calculated according to Eq. (4), as all the current is assumed to go through the pits at the affected cracks.

$$i_1 = \frac{I_{eff}}{S_{pit}} = \frac{I_{eff}}{\phi\pi\sum L_{pit}} \quad (4)$$

where S_{pit} is the surface area subjected to corrosion, ϕ is the diameter of the steel bar before corrosion and $\sum L_{pit}$ is the sum of all the individual pit lengths, calculated according to [30] and further described in section 2.3, and assuming that this length is invariant over time as described in the second assumption.

According to the underlying hypothesis, the computation of current densities at later stages $i_j(k_j(t))$, when the slope of the deflection curve changes, could then be conducted according to Eq. (5):

$$i_j(k_j(t)) = i_1 \frac{k_j(t)}{k_1} \quad (5)$$

.

Under these considerations, the total steel volume loss in the pits,

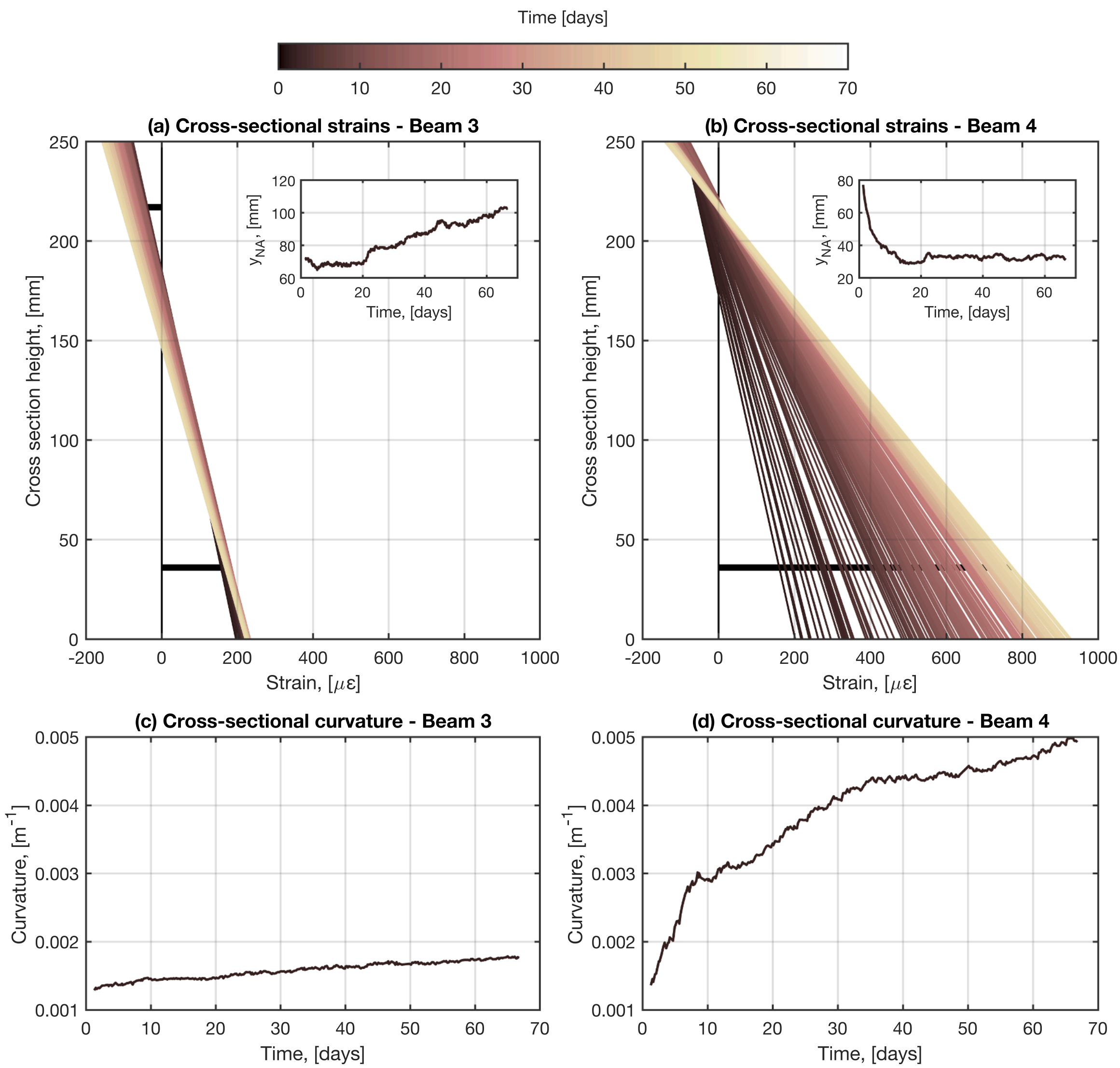

Fig. 7. **(a, b)** Cross-sectional strains and distance to the neutral axis for load cycles $F_L = 6$ kN, in beam 3 (uncorroded) and beam 4 (corroded) from [27]; **(c, d)** Cross-sectional curvature for load cycles $F_L = 6$ kN, in beam 3 (uncorroded) and beam 4 (corroded) from [27].

C_{pits}, is computed through Faraday's law, according to Eq. (6):

$$C_{pit} = \frac{MS_{pit}}{\rho Fz} \int_0^t i_j\left(k_j(t)\right) dt \tag{6}$$

.

A more detailed description of the framework can be found in [27].

4. Results and discussion

4.1. Application and extension of the proposed framework

In this section the application of the framework is examined. Although calculations were performed for all corroded beams in Series 2, only beam 5-s2 is presented as a representative example. The uncorroded reference beam 1-s2 is used to remove the deflection contribution from creep, and the 3D scanning results from beam 5-s1 are included to compare the corrosion distribution between the two series.

4.1.1. Corrosion distribution from 3D scanning

The 3D scanning results of the reinforcement bars from beam 5-s1 and beam 5-s2 are presented in Fig. 3a and Fig. 3b, respectively. Strains measured with the DOFS during a high load cycle are included to indicate the locations of the pitting regions, using the pit length definition introduced in Section 2.3. Moreover, the pit corrosion volumes are shown in the figure at each pit. According to the first assumption in Section 3, a pronounced localization of corrosion at the bending cracks was anticipated for Series 1, since those tests were terminated when longitudinal corrosion cracks occurred. Contrary to this expectation, the pitting corrosion observed in Fig. 3a was less pronounced than that reported in the authors' previous study [27] in which the framework for cyclically loaded beams was established and distinct pitting corrosion was observed at the bending cracks. One possible explanation is the difference in chloride diffusion coefficients, which can be attributed to the younger concrete age in the present study. Luping [31] developed a model for chloride ingress in submerged marine concrete and laboratory tests showed that the chloride diffusion coefficient decreases over time and stabilizes after approximately 6 months. The beam in [27] was approximately one year old, compared with 28 days in the present study.

In Table 2, the 3D scanning results are shown for all beams, including the total volume loss, the volume loss in the pits, and the ratio between them. Moreover, the effective currents according to Eq. (3) are presented. Consistent with the previously mentioned assumption, Series 2 was expected to have a more uniform corrosion pattern than Series 1 due to the formation of longitudinal cracking. However, the differences are

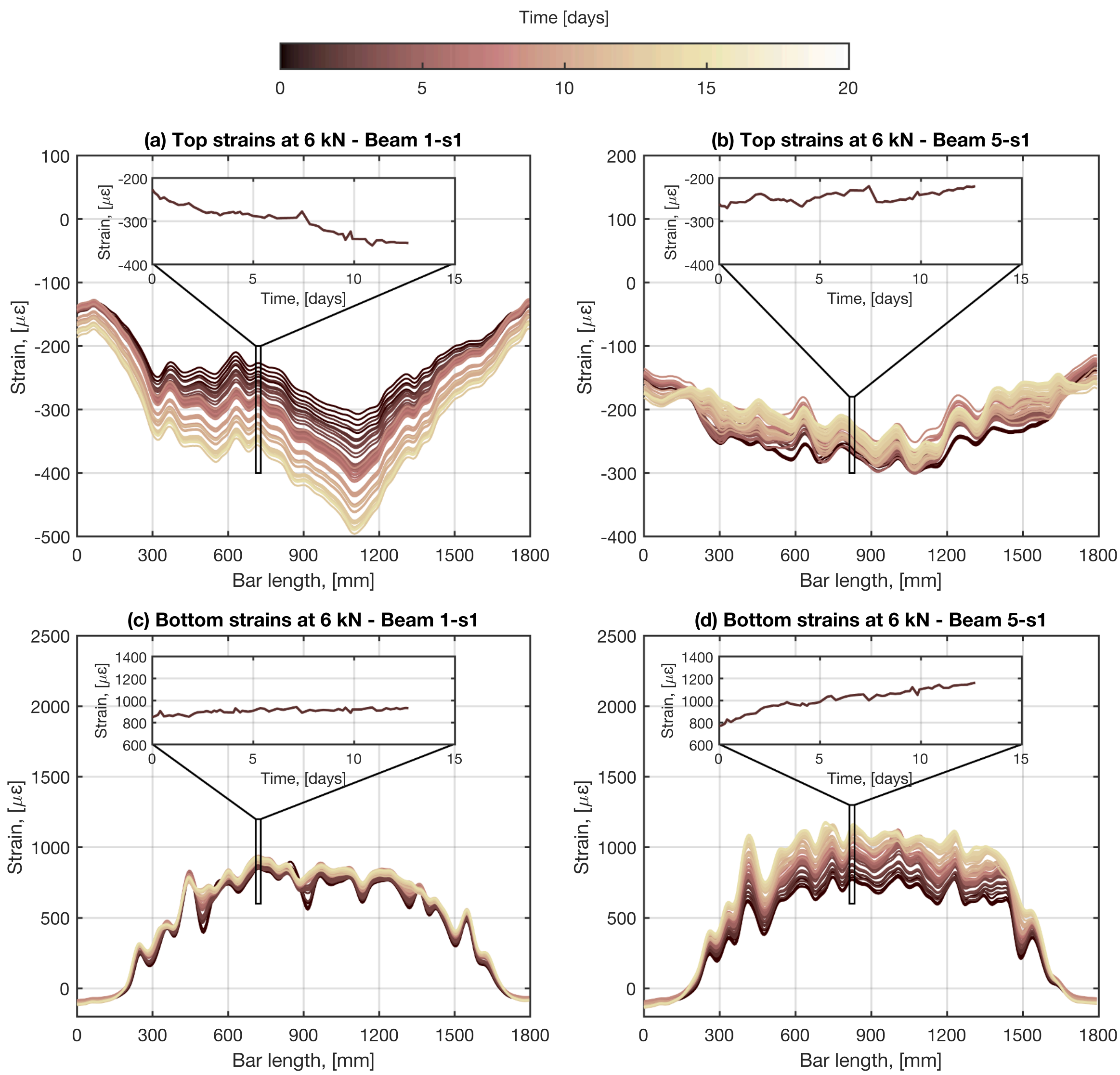

Fig. 8. **(a, b)** Strains along the top reinforcement bar for load cycles $F_L = 6$ kN, in beam 1-s1 (uncorroded) and beam 5-s1 (corroded); **(c, d)** Strains along the bottom reinforcement bar for load cycles $F_L = 6$ kN, in beam 1-s1 (uncorroded) and beam 5-s1 (corroded).

largely negligible, and in one case, beam 5-s1 compared to beam 5-s2, the trend is even reversed, with Series 1 showing a more uniform corrosion distribution. Apart from the expected observation that beams with larger corroded regions experienced greater steel loss, no apparent effect on the corrosion morphology was observed for the varied parameters in this study, namely reinforcement bar diameter and number of bars.

4.1.2. *Corrosion-induced variations in deflections*

Fig. 4 presents the incremental midspan deflection starting from the first low-load cycle, $F_L = 6$ kN, for one representative beam pair from each series. The shaded areas indicate periods when the hydraulic pump was malfunctioning, and the specimens were consequently unloaded.

For Series 2, the corroded specimen exhibits smaller deflections at the higher load levels than the uncorroded reference, even during the initial cycles preceding any corrosion, as shown in Fig. 4b. No definitive explanation for this behavior has been identified. The specimen geometry was the same, and the only difference in the test setup was the use of a shared DOFS for the beam pairs, achieved by splicing the fiber between the uncorroded reference beam and the corroded beam. Although the splice is not expected to influence the strain measurements, erroneous strain data remain the most plausible explanation, rather than errors in the deflection calculation method, which has been verified against digital image correlation by several authors [32,33].

Nevertheless, when applying the framework, only the change in slope of the low load cycles, $F_L = 6$ kN, is utilized, after removing creep by subtracting the deflection of the uncorroded reference beam. Therefore, the anomalous behavior during the higher load cycles is not expected to influence the calculation of steel losses.

The framework was not applied to the beams in Series 1 because no change in the slope of the deflection curve for the low load cycles was observed prior to the onset of longitudinal cracking, which is a condition for estimating the current densities at later stages. Since the effective impressed current used in the framework is, in this case, derived directly from the results of the 3D scanning, the computed steel loss would equal the 3D-scanned volume.

Fig. 5 summarizes the results from the framework for beam 5 from Series 2. In Fig. 5a, the midspan deflection of the uncorroded reference beam is subtracted from the corroded beam to isolate the corrosion-induced component by removing the creep. The negative increments arise from differences in the unloaded response between the corroded and reference beams. An explanation for the discrepancies could be that the self-weight acts in the opposite direction to the applied load on the corroded beam. By contrast, in the uncorroded beam the self-weight acts

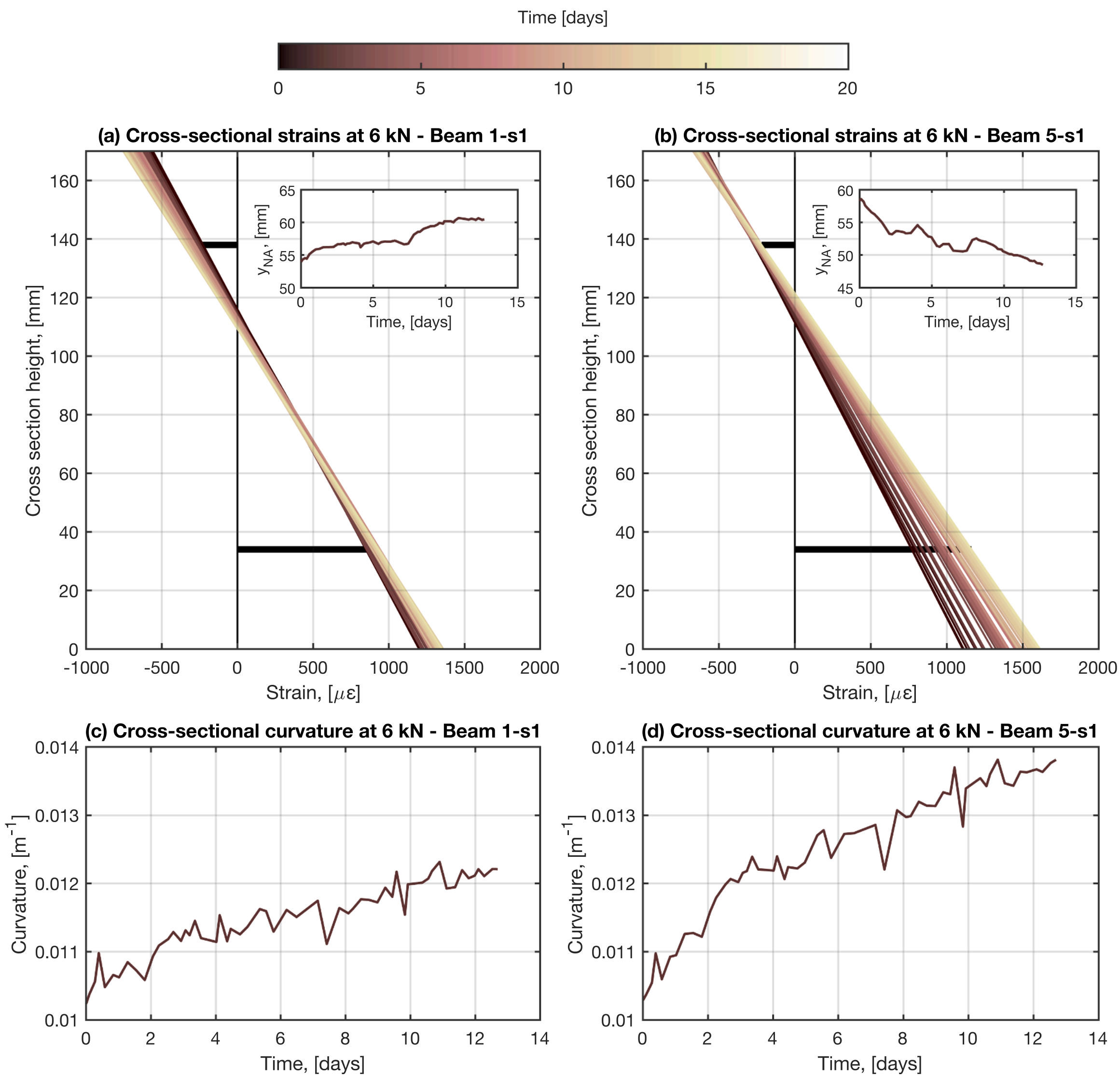

Fig. 9. (a, b) Cross-sectional strains and distance to the neutral axis for load cycles $F_L = 6$ kN, in beam 1-s1 (uncorroded) and beam 5-s1 (corroded), respectively; (c, d) Cross-sectional curvature for load cycles $F_L = 6$ kN, in beam 1-s1 (uncorroded) and beam 5-s1 (corroded).

in the same direction as the applied load, resulting in larger creep deformations. Consequently, upon resumption of loading, the deflections recorded during the subsequent load cycles were larger.

Due to problems with the ODiSI equipment, no strain data were recorded during the first two days of testing. To account for the fact that the impressed current and cyclic loading were applied during this period, the initial current density was applied from $t = -2$ days in Fig. 5c and Fig. 5d. With this adjustment, longitudinal cracking was observed about 14 days from the start of the impressed current application.

Application of the framework yielded a final value of the pitting corrosion $C_{tot,pit} = 2375$ mm^3, which is 19% below the value obtained from the 3D scanning, $C_{pit,scan} = 2914$ mm^3. As previously indicated, this discrepancy is mainly attributed to the corrosion being more uniformly distributed than expected, especially in the initial phase before longitudinal cracking, which is the one used to define the initial parameters of the framework.

The calculated pitting corrosion losses, together with the losses from the 3D scanning, are presented in Table 3 for all Series 2 beams. In every case, the calculated values are smaller than the 3D-scanned losses. However, beam 7-s2 and beam 8-s2, which were reinforced with 3ϕ10 bars, showed closer agreement with the 3D-scanned volume loss.

4.2. Strain and curvature distribution and evolution

In this section, the strain development is studied in detail at a representative cracked cross-section to investigate the effects of corrosion on the cross-sectional response.

For context and direct comparison with the experiments presented in this paper, the cyclically loaded beam from [27] is analyzed first. The strains along the corroded constant-moment region are presented in Fig. 6. In the uncorroded reference beam, the bottom-fiber strains, shown in Fig. 6c, remain essentially unchanged, whereas the top-fiber strains trend toward more negative, i.e. compressive, values with time. The observed strain evolution matches the expected time-dependent response under cyclic loading. In particular, the progressive increase in compressive strains is consistent with creep of concrete in compression.

In the corroded beam, the top-fiber strains in Fig. 6b become more positive until approximately day 13, after which they stabilize. The bottom-fiber strains depicted in Fig. 6d, in contrast, increase throughout the corrosion process with distinct slope changes that mirror the piecewise increases in deflection.

The cross-sectional strain distributions at the cracks shown in Fig. 6 are presented in Fig. 7a and Fig. 7b, for the uncorroded and corroded

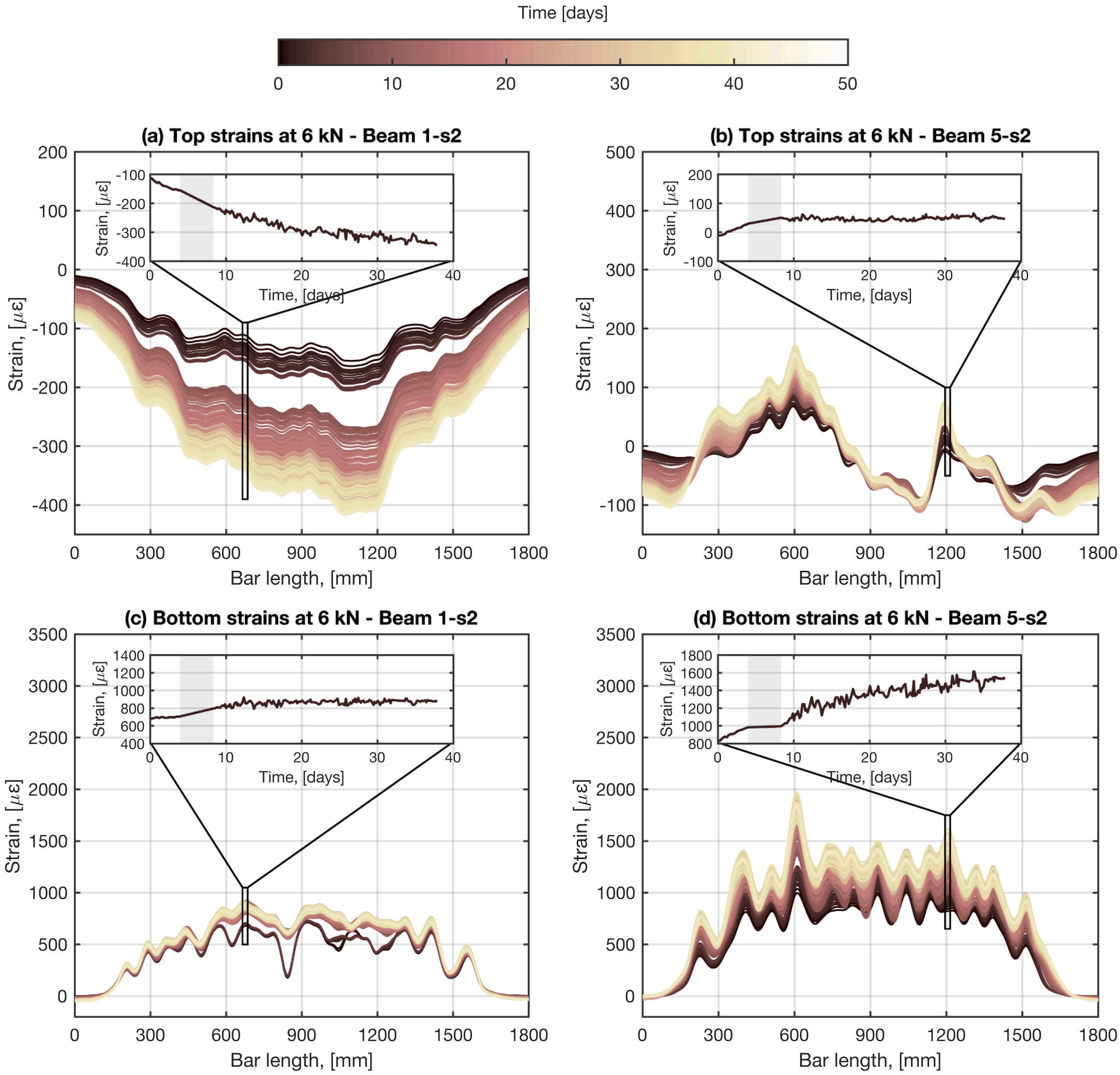

Fig. 10. (a, b) Strains along the top reinforcement bar for load cycles $F_L = 6$ kN, in beam 1-s2 (uncorroded) and beam 5-s2 (corroded); **(c, d)** Strains along the bottom reinforcement bar for load cycles $F_L = 6$ kN, in beam 1-s2 (uncorroded) and beam 5-s2 (corroded).

beams respectively, together with the neutral-axis depth measured from the top surface. Fig. 7c and Fig. 7d depict the resulting curvature distributions for the uncorroded and corroded beam respectively. In the corroded beam, the depth of the neutral axis decreases before becoming effectively stationary after about 13 days, coincident with the stabilization of the top-fiber strains and the onset of longitudinal cracking. In the uncorroded beam, the neutral-axis depth increases over time, reflecting creep-driven growth in the top-fiber compressive strains.

Once longitudinal cracking develops, the bond and tension-stiffening effects are significantly reduced. Combined with the loss of steel area, a higher steel strain is required to achieve the same tensile force, leading to continued growth of bottom-fiber strains to maintain equilibrium while the compressive force in the top reinforcement remains more or less constant. However, the decrease in compressive strain prior to longitudinal cracking is somewhat unexpected, since increasing tensile strains before bond degradation should be accompanied by a rise in compressive force to maintain equilibrium. The results suggest that the non-mechanical tensile strains induced by corrosion are transferred to the rest of the cross-section and influence the strains in the top fiber. Once the bond is degraded due to longitudinal cracking this transfer mechanism is lost, and together with the previously mentioned factors, the top-fiber strains stabilize. A similar behavior, with an initial decrease of compressive strains and neutral axis depth before stabilization, was reported in [17] for the corroded beam with transversal cracks.

Fig. 8 depicts the strains along the entire span for a representative pair of beams from Series 1, with results generally in agreement with the pre-longitudinal-cracking behavior in Fig. 6. For the uncorroded reference beam, the top-fiber strains shown in Fig. 8a become increasingly compressive across the span. Another observation emerges when examining the strains along the entire span. The top-fiber strains become less compressive only within the corroded region, from about 200 mm to about 1400 mm, while the uncorroded regions behave similarly to the reference beam. This pattern further supports a corrosion-induced redistribution of strains before longitudinal cracking.

The strains at the cracked sections presented in Fig. 8 were used to determine the cross-sectional strain distributions and curvatures shown in Fig. 9. For the uncorroded beam, increases are observed in the neutral-axis depth, shown in Fig. 9a, and in the curvature presented in Fig. 9c, in agreement with the response observed in Fig. 7. Moreover, the corroded beam from Series 1 shows a similar response to that observed in Fig. 7, prior to the longitudinal cracking of the corroded beam. The depth of the neutral axis, shown in Fig. 9b, decreases, whereas the curvature, presented in Fig. 9d, increases more rapidly than in the reference beam.

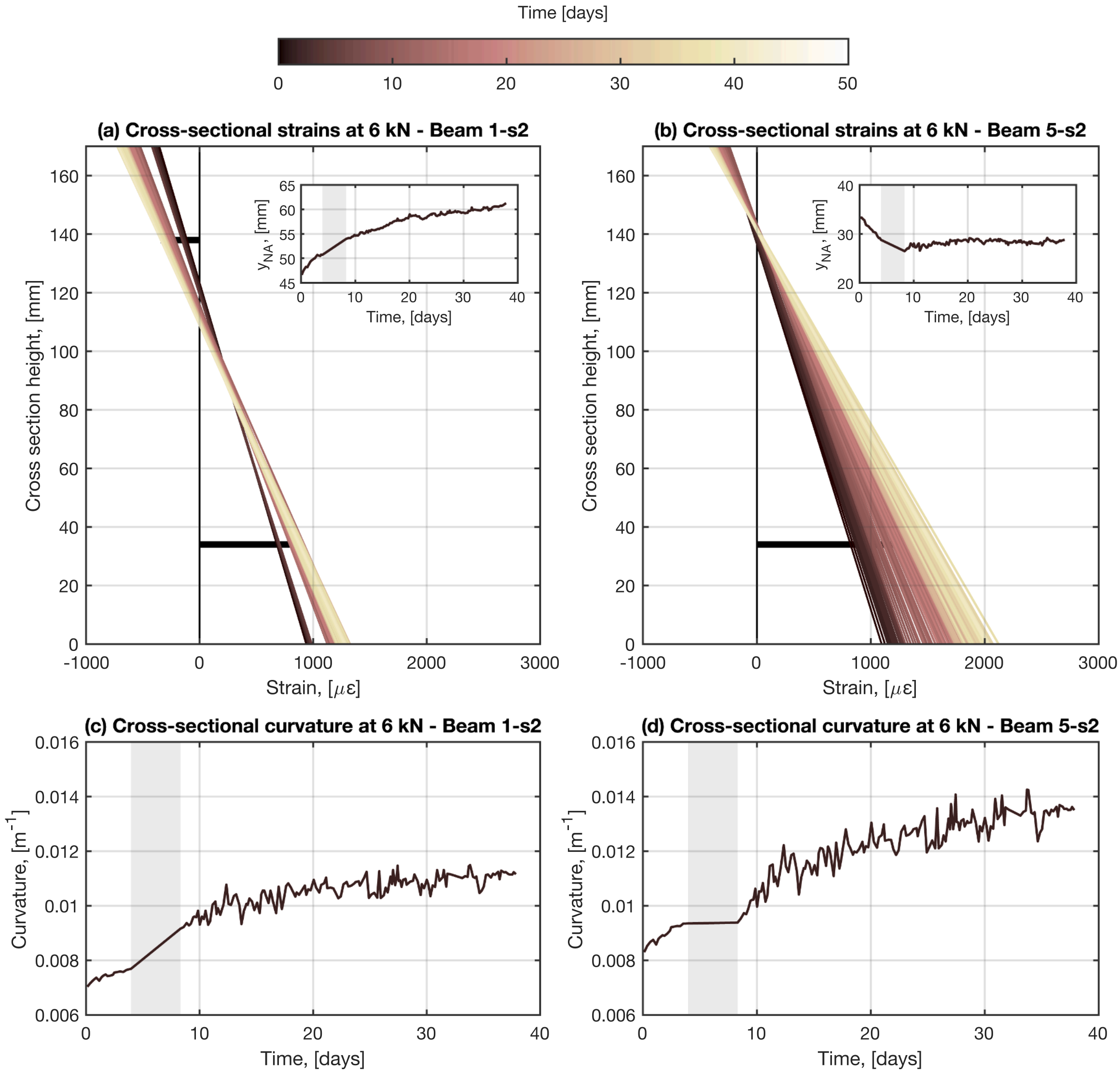

Fig. 11. **(a, b)** Cross-sectional strains and distance to the neutral axis for load cycles $F_L = 6$ kN, in beam 1-s2 (uncorroded) and beam 5-s2 (corroded); **(c, d)** Cross-sectional curvature for load cycles $F_L = 6$ kN, in beam 1-s2 (uncorroded) and beam 5-s2 (corroded).

The strain profiles of a Series 2 beam pair, with the same reinforcement layout and corroded region as those in Fig. 8, are plotted in Fig. 10. Before longitudinal cracking, that is the period preceding the shaded area marking the hydraulic pump malfunction, the behavior matches that observed in Series 1. In the uncorroded reference beam, the top-fiber strains shown in Fig. 10a become progressively more compressive across the span, whereas the top-fiber strains in the corroded beam, presented in Fig. 10b, trend toward more positive values in the corroded region. Furthermore, the bottom-fiber strains remain almost constant for the uncorroded beam, displayed in Fig. 10c, in contrast to the increasing bottom-fiber strains in the corroded beam, shown in Fig. 10d. Subsequent to longitudinal cracking, the corroded beam behaves as in Fig. 6, with stable top-fiber strains and increasing bottom-fiber strains.

Unlike the previously presented specimens, the bottom-fiber strains in the uncorroded beam increase, while remaining constant in the corroded beam, when the beams were not subjected to cyclic loading. This difference may be due to the test setup. The uncorroded beam was positioned above with its bottom side downward, whereas the corroded beam was placed below with its bottom side upward, meaning that the self-weight acted in different directions relative to the previously applied load.

The cross-sectional strain and curvature distributions are plotted in Fig. 11. For the uncorroded beam, consistent with previous results, the neutral-axis depth and curvature, shown in Fig. 11a and Fig. 11c respectively, increase over the course of the test. Moreover, the corroded beam behaves similarly to the case in Fig. 7, where the neutral-axis depth, depicted in Fig. 11b, decreases and then remains essentially constant, stabilizing around the formation of longitudinal cracks. The curvature response in Fig. 11d reflects this trend.

One difference between the results for the beams in Series 2 and those in the previous study [27] is that the flattening of peaks and valleys during the low load cycles after longitudinal cracking, as shown in Fig. 6d, was not observed. However, the Series 1 and Series 2 beams had lower capacities than those in [27], while the same load level was applied during unloading. As a result, the cracks remained more open.

4.3. Calculation of Young's modulus from cross-sectional strain distributions

In Fig. 12, the cross-sectional strains from Section 4.2 are used, together with Navier's formula and an equivalent cross-section, to compute an apparent Young's modulus that gives zero stress at the neutral axis. The stiffness reduction associated with the loss of cross-

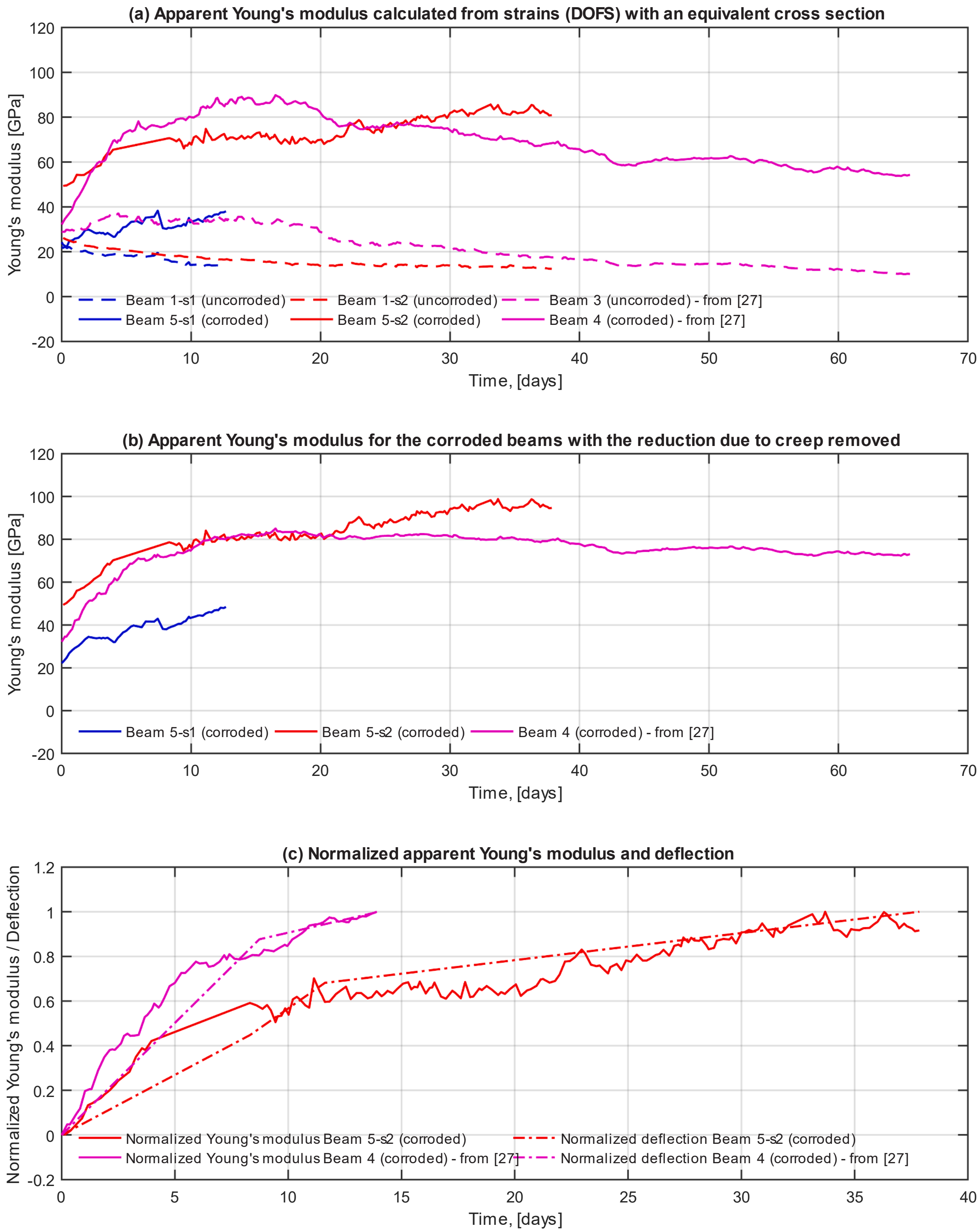

Fig. 12. **(a)** Apparent Young's modulus for the uncorroded and corroded beams; **(b)** Apparent Young's modulus for the corroded beams with creep reduction removed; **(c)** Normalized apparent Young's modulus and normalized idealized deflection curves.

sectional area was negligible, and the uncorroded reinforcement bar area was therefore used in all calculations. The uncorroded beams, shown in Fig. 12a, have reasonable values of the initial apparent Young's modulus of about 25–30 GPa, which subsequently decrease over time consistent with the expected effects of creep. The apparent Young's modulus of the corroded beam 5 from Series 1 exhibits the same behavior as beam 4 in [27] prior to longitudinal cracking, starting at a value similar to its uncorroded reference and then increasing significantly over time. The Series 2 corroded beam exhibits the same trend. However, the initial apparent Young's modulus is much higher, about 50 GPa, likely attributable to the cause of the inaccurate strain data leading to the unrealistic deflections observed in Fig. 4b. In contrast to beam 4, the apparent Young's modulus for beam 5 from Series 2 starts increasing once more after being constant for roughly ten days following longitudinal cracking. In Fig. 12b, the apparent Young's moduli for the corroded beams are presented, with the reduction due to creep excluded using the results for the uncorroded beams. Despite increasing to more than twice the initial values, and not reflecting the actual material properties, the apparent Young's modulus from the sectional analysis provides a useful indicator of corrosion, since the values for the uncorroded reference beams remain within a reasonable range. To further validate the apparent Young's modulus as an indicator of corrosion, it is presented in Fig. 12c together with the idealized deflection curves from Section 4.1.2 for Beam 5-s2 and from [27] for Beam 4. The deflection curve presented in Section 4.1.2 was adjusted following the hydraulic pump malfunction to ensure continuity. Subsequently, to facilitate comparison between the slope changes of the deflection curves and the apparent Young's modulus, only the response up to the maximum Young's modulus value, prior to stabilization, is included. Furthermore, both curves were normalized to improve the comparison. The reasonably good agreement between the slope changes further supports the use of the apparent Young's modulus as an indicator of corrosion.

5. Conclusions

In this study, the previously proposed framework from [27] for describing corrosion propagation based on corrosion-induced deflection in RC beams was extended and validated under a wider range of conditions. Furthermore, the strain development was studied at a representative cracked cross-section, to investigate the effects of corrosion on the cross-sectional response and to calculate an apparent Young's modulus.

The results showed that the framework becomes less accurate when the corrosion distribution is relatively uniform rather than characterized by distinct pitting corrosion. Although the experimental setup was designed to promote non-uniform corrosion, the more uniform corrosion observed in the present study was attributed to the young age of the concrete at the start of testing. Moreover, the non-mechanical corrosion-induced strains were found to transfer through the height of the cross-section until longitudinal cracking occurred. Consequently, the top-fiber strains in the corroded region became less compressive up to the onset of cracking, after which they stabilized and remained approximately constant, while the bottom-fiber strains continued to increase. In contrast, the top strains in the uncorroded region became more compressive, consistent with the creep behavior observed in the uncorroded reference beam. Finally, the apparent Young's modulus calculated using Navier's formula and an equivalent cross-section was shown to be a useful indicator of corrosion progression, although it does not represent the actual material properties.

The proposed framework is currently limited to the assessment of global corrosion, represented by the total corrosion damage from all corrosion pits, and does not account for the effects of local corrosion. Extending the framework to capture localized corrosion damage therefore represents an important direction for future research. In addition, the framework is presently more applicable when the corrosion distribution is characterized by distinct pitting corrosion rather than uniform corrosion. Since naturally corroded reinforcement bars typically exhibit distinct localized pitting, further investigations considering naturally developed corrosion patterns are necessary to improve the applicability of the framework to real structural conditions.

Furthermore, the cross-sectional analysis demonstrated that corrosion-induced non-mechanical strains significantly influence the structural response and therefore need to be considered when evaluating the behavior of corroded RC beams. Incorporating these effects is important for achieving a more accurate representation of the serviceability response of corroded structures.

Funding

This research has been performed as part of the project: 'Shedding light on internal damage: fiber optic-driven condition assessment of corroded concrete structures' funded by the Swedish government research council Formas under the grant 2021–01103_Formas.

CRediT authorship contribution statement

Ignasi Fernandez: Writing – review & editing, Supervision, Methodology, Funding acquisition, Conceptualization. **Carlos G. Berrocal:** Writing – review & editing, Supervision, Methodology, Conceptualization. **Rasmus Rempling:** Writing – review & editing, Supervision, Methodology, Conceptualization. **David Dackman:** Writing – original draft, Visualization, Methodology, Conceptualization.

Declaration of Competing Interest

The authors declare that they have no known competing financial interests or personal relationships that could have appeared to influence the work reported in this paper.

References

[1] Kopiika N.S., Ninic J., Cucuzza R., Mitoulis S.A."Deterioration rate diagnosis to global climatic change: The case of Dnipro Dam in Ukraine," Bridge Maintenance, Safety, Management, Digitalization and Sustainability - Proceedings of the 12th International Conference on Bridge Maintenance, Safety and Management, IABMAS 2024, pp. 2603–2611, 2024, doi: 10.1201/9781003483755-310..

[2] Kopiika N, Robery P, Ninic J, Mitoulis SA. "Remaining life of ageing RC infrastructure for sustainable development—deterioration under climate change," (no. May) Case Stud Constr Mater 2025;22. https://doi.org/10.1016/j.cscm.2025.e04757.

[3] Bonacci JF, Maalej M. "Externally-bonded FRP for service-life extension of RC infrastructure,". J Infrastruct Syst 2000;6(1):41–51.

[4] Anusha G, Rajan D. "An integrated service life prediction model for chloride-induced corrosion in reinforced concrete structures,". Eur J Environ Civil Eng 2025;30(1):1–22. https://doi.org/10.1080/19648189.2025.2551982.

[5] Hao S, Ph D, Asce M. "I-35W Bridge Collapse. J Bridge Eng 2010;15(5):608–14.

[6] Morgese M, Ansari F, Domaneschi M, Cimellaro GP. "Post-collapse analysis of Morandi's Polcevera viaduct in Genoa Italy,". J Civ Struct Health Monit 2020;10 (1):69–85. https://doi.org/10.1007/s13349-019-00370-7.

[7] Iannuzzi M, Frankel GS. "The carbon footprint of steel corrosion,". Npj Mater Degrad 2022;6(1):1–4. https://doi.org/10.1038/s41529-022-00318-1.

[8] Tahershamsi M, Fernandez I, Lundgren K, Zandi K. "Investigating correlations between crack width, corrosion level and anchorage capacity,". Struct Infrastruct Eng 2017;13(10):1294–307. https://doi.org/10.1080/15732479.2016.1263673.

[9] Hariche L, Ballim Y, Bouhicha M, Kenai S. "Effects of reinforcement configuration and sustained load on the behaviour of reinforced concrete beams affected by reinforcing steel corrosion,". Cem Concr Compos 2012;34(10):1202–9. https://doi.org/10.1016/j.cemconcomp.2012.07.010.

[10] Kopiika N, Blikharskyy Y, Selejdak J, Khmil R, Blikharskyy Z. "Reliability-based analysis and residual life forecasting for corrosion-affected RC structures," (no. April) Structures 2025;76:108965. https://doi.org/10.1016/j.istruc.2025.108965.

[11] Stein KJ, Graeff ÂG, Garcez MR. "Structural performance of reinforced concrete beams subjected to combined effects of corrosion and cyclic loading," (Jun) J Build Pathol Rehabil 2023;8(1). https://doi.org/10.1007/s41024-022-00263-1.

[12] Oh BH, Asce M, Kim SH. "Realistic models for local bond stress-slip of reinforced concrete under repeated loading,". J Struct Eng 2007;133(2):216–24. https://doi.org/10.1061/ASCE0733-94452007133:2216.

[13] Zhou HJ, Liang XB, Zhang XL, Lu JL, Xing F, Mei L. "Variation and degradation of steel and concrete bond performance with corroded stirrups,". Constr Build Mater May 2017;138:56–68. https://doi.org/10.1016/j.conbuildmat.2017.02.007.

[14] Dasar A, Patah D, Hamada H, Yamamoto D, Sagawa Y. "Life performance of 40-year-old RC beams with different concrete covers and bar diameters in natural corrosion environments," (no. November) Structures 2022;46:2031–46. https://doi.org/10.1016/j.istruc.2022.11.033.

[15] Zhang R, Castel A, François R. "The corrosion pattern of reinforcement and its influence on serviceability of reinforced concrete members in chloride environment,". Cem Concr Res 2009;39(11):1077–86. https://doi.org/10.1016/j.cemconres.2009.07.025.

[16] Fang C, Gylltoft K, Lundgren K, Plos M. "Effect of corrosion on bond in reinforced concrete under cyclic loading," (Mar) Cem Concr Res 2006;36(3):548–55. https://doi.org/10.1016/j.cemconres.2005.11.019.

[17] Malumbela G, Moyo P, Alexander M. "Behaviour of RC beams corroded under sustained service loads,". Constr Build Mater 2009;23(11):3346–51. https://doi.org/10.1016/j.conbuildmat.2009.06.005.

[18] Fernandez I, Berrocal CG, Rempling R. "Two-dimensional strain field analysis of reinforced concrete D-regions based on distributed optical fibre sensors," (Mar) Eng Struct 2023;278. https://doi.org/10.1016/j.engstruct.2022.115562.

[19] Richter B, Herbers M, Marx S. "Crack monitoring on concrete structures with distributed fiber optic sensors—Toward automated data evaluation and assessment,". Struct Concr 2024;25(2):1465–80. https://doi.org/10.1002/suco.202300100.

[20] Wang S, et al. Distributed fiber optic sensing for internal strain monitoring in full life cycle of concrete slabs with BOFDA technology (no. January) Eng Struct 2024;305:117798. https://doi.org/10.1016/j.engstruct.2024.117798.

[21] Rodríguez G, Casas JR, Villaba S. "Cracking assessment in concrete structures by distributed optical fiber,". Smart Mater Struct 2015;24(3). https://doi.org/10.1088/0964-1726/24/3/035005.
[22] Fernandez I, Berrocal CG, Rempling R. "Long-term performance of distributed optical fiber sensors embedded in reinforced concrete beams under sustained deflection and cyclic loading,". Sensors 2021;21(19). https://doi.org/10.3390/s21196338.
[23] Hüsken G, Pirskawetz S, Hofmann D, Basedau F, Gründer KP, Kadoke D. "The load-bearing behaviour of a reinforced concrete beam investigated by optical measuring techniques,". Mater Struct/Mater Et Constr 2021;54(3). https://doi.org/10.1617/s11527-021-01699-6.
[24] Bado MF, Casas JR, Kaklauskas G. "Distributed Sensing (DOFS) in Reinforced Concrete members for reinforcement strain monitoring, crack detection and bond-slip calculation," (Jan) Eng Struct 2021;226. https://doi.org/10.1016/j.engstruct.2020.111385.
[25] Fan L, Tan X, Zhang Q, Meng W, Chen G, Bao Y. "Monitoring corrosion of steel bars in reinforced concrete based on helix strains measured from a distributed fiber optic sensor," (Feb) Eng Struct 2020;204. https://doi.org/10.1016/j.engstruct.2019.110039.
[26] Dackman D, Fernandez I, Berrocal CG, Rempling R. "Correlations between localized pitting corrosion and deflection in reinforced concrete beams subjected to accelerated corrosion,". Int RILEM Conf Synerg Expert Towards Sustain Robust Cem-Based Mater Concr Struct 2023:902–12.
[27] Dackman D, Berrocal CG, Rempling R, Fernandez I. "A framework for evaluating steel loss from the evolution of corrosion-induced deflections in reinforced concrete beams with non-uniform reinforcement corrosion," (no. May) Eng Struct 2024;317:118593. https://doi.org/10.1016/j.engstruct.2024.118593.
[28] Fernandez I, Lundgren K, Zandi K. "Evaluation of corrosion level of naturally corroded bars using different cleaning methods, computed tomography, and 3D optical scanning,". Mater Struct/Mater Et Constr 2018;51(3):1–13. https://doi.org/10.1617/s11527-018-1206-z.
[29] Tahershamsi M, Fernandez I, Lundgren K, Zandi K. "Investigating correlations between crack width, corrosion level and anchorage capacity,". Struct Infrastruct Eng 2017;13(10):1294–307. https://doi.org/10.1080/15732479.2016.1263673.
[30] Berrocal CG, Fernandez I, Rempling R. "The interplay between corrosion and cracks in reinforced concrete beams with non-uniform reinforcement corrosion,". Mater Struct/Mater Et Constr 2022;55(4):1–16. https://doi.org/10.1617/s11527-022-01956-2.
[31] Luping T. "Engineering expression of the ClinConc model for prediction of free and total chloride ingress in submerged marine concrete,". Cem Concr Res 2008;38(8–9):1092–7. https://doi.org/10.1016/j.cemconres.2008.03.008.
[32] Berrocal CG, Fernandez I, Bado MF, Casas JR, Rempling R. "Assessment and visualization of performance indicators of reinforced concrete beams by distributed optical fibre sensing,". Struct Health Monit 2021;20(6):3309–26. https://doi.org/10.1177/1475921720984431.
[33] Wiater A, Ziaja D, Kulpa M, Siwowski T. "Comparison of distributed fiber optic sensing and digital image correlation measurement techniques for evaluation of flexural behavior of cfrp-prestressed concrete beams,". Sensors 2025;25(23):1–25. https://doi.org/10.3390/s25237357.